



## Article

# Modelling, Design and Validation of Spatially Resolved Reflectance Based Fiber Optic Probe for Epithelial Precancer Diagnostics

Pankaj Singh <sup>1,2,†</sup> , Prabodh Pandey <sup>1</sup>, Shivam Shukla <sup>3</sup>, Naren Naik <sup>3,4</sup>  
and Asima Pradhan <sup>1,3,\*</sup> 

<sup>1</sup> Department of Physics, Indian Institute of Technology Kanpur, Kanpur 208016, India; singhp@iitk.ac.in (P.S.); prabodh@iitk.ac.in (P.P.)

<sup>2</sup> Department of Physics, Laxman Singh Mahar Government Post Graduate College, Pithoragarh 262502, India

<sup>3</sup> Center for Lasers and Photonics, Indian Institute of Technology Kanpur, Kanpur 208016, India; sshivam@iitk.ac.in (S.S.); nnaik@iitk.ac.in (N.N.)

<sup>4</sup> Department of Electrical Engineering, Indian Institute of Technology Kanpur, Kanpur 208016, India

\* Correspondence: asima@iitk.ac.in

† Author majorly contributed to this work.

Received: 29 September 2020; Accepted: 9 November 2020; Published: 10 December 2020



**Abstract:** Fiber-optic probes are imperative for in-vivo diagnosis of cancer. Depending on the access to a diseased organ and the mutations one aims to sense, the probe designs vary. We carry out a detailed numerical study of the efficacy of the common probe geometries for epithelial cancer characterization based on spatially resolved reflectance data. As per the outcomes of this comparative study, a probe has been manufactured and using Monte Carlo look up table based inversion scheme, the absorption and scattering coefficients of the epithelium mimicking top layer have been recovered from noisy synthetic as well as experimental data.

**Keywords:** optical parameters; beveled fiber; spatially resolved reflectance; epithelial pre-cancer; look-up table

## 1. Introduction

About 80–90% of human cancers develop in the epithelium layer [1] where early signs of the disease appear [2–4]. The early signs manifest in its optical properties, making it crucial to probe the epithelium in order to diagnose pre-cancer. The epithelium layer is the outermost layer of skin and typically 100–500  $\mu\text{m}$  thick [2]. To optically probe the changes occurring in the epithelium layer, one needs to collect the photons which have had interactions predominantly in the epithelium layer. Therefore, it becomes important to understand the geometries of collection and delivery of light which govern depth selection. Typical elements of probe geometry include source-detector separation (SDS), and angular orientation of incidence and collection of light. In this context, a common technique for probing various depths is spatially resolved reflectance (SRR). In SRR, light beam incident on the tissue interacts with cellular components and is collected after absorption and scattering inside the medium, at different spatial positions. This technique allows one to probe various depths inside the tissue through the spatially collected light. SRR based technique was first proposed by Farrell et al. [5] in 1992 to non-invasively recover the optical parameters of the tissue. Similarly, spatially resolved fluorescence has also been used to recover the optical properties of tissues [6,7].

For clinical applications, fiber-based SRR probes are desirable. One of the early developments of SRR based fiber optic probe was by Bays et al. [8]. This probe consisted of six detector fibers with the closest detector placed at 2.0 mm from the source. They implemented a diffusion approximated

radiative transport equation (DA-RTE) based model to quantify the optical properties of the epithelial tissue. For an epithelial tissue, diffusion approximation does not hold good close to the source. Therefore, a large variance ( $\sim 30\%$ ) was observed in the recovered optical parameters reported by them. In another study [9], a fiber optic probe was incorporated for SRR collection from a two-layered phantom with a 6 mm thick upper layer. For such a phantom where the thickness of the top layer is significantly larger than the optical mean free path [10], diffuse photons are observed in the superficial layer itself due to large number of scattering events (greater than 100). Therefore, using DA-RTE-based recovery, while 23% error in the optical parameters was obtained for a 2 mm thick superficial layer, the error reduces to 8% for a 10 mm thick superficial layer.

In 2011, Tseng et al. [4] designed a probe consisting of a source fiber of diameter 200  $\mu\text{m}$  and 7400 bundled plastic fibers of diameter 20  $\mu\text{m}$  for SRR collection and extracted the optical parameters of homogeneous phantoms with about 6% and 4.3% errors in absorption and scattering coefficients respectively. Subsequently numerical studies were carried out on two layer models, and the optical parameters of epithelium and stroma were extracted separately.

All the fiber optic probes discussed above were oriented perpendicular to the collection surface. These studies are not suitable for recovering the optical properties of a thin epithelium layer (200–500  $\mu\text{m}$ ) because the SRR collected in the perpendicular geometry has a low sensitivity [11,12] to epithelial perturbations. Moreover, these studies utilized diffusion approximations (DA-RTE) for recovery of the optical parameters which does not hold for epithelial tissue. It is thus crucial to evaluate various feasible probe geometries as well as use the complete RTE as the photon transport model for recovering optical parameters of the epithelial tissue. Several groups across the globe have carried out Monte-Carlo (MC) simulations to evaluate geometries for optimal designing of a probe for epithelial precancers. A detailed study of various fiber-optic probe geometries can be found in [13]. Liu et al. [3] and Wang et al. [12] reported significant improvements by using oblique fibers, observing higher sensitivity to changes in the epithelium layer during measurements. Liu et al. [3] used an inverse MC scheme to obtain the optical properties of the top layer by a  $45^\circ$  angled probe, and bottom layer optical properties with a flat tipped probe. However, the geometries for angled probes that they proposed are not amenable for internal organs due to critical issues with fibers while bending to a smaller radius [14].

Sung et al. [11] in 2012, carried out a MC based comparative numerical study for various probe geometries. They reported that the perpendicular probe was more sensitive to the changes in stromal optical properties. However, the changes in epithelial scattering were reflected more prominently by the parallel-oblique fiber probe. Such a probe is suitable for epithelial precancer investigation and also clinically amenable.

In 2014, Sung et al. [15] measured SRR spectra using perpendicular as well as a  $45^\circ$  beveled optical fiber bundle. They used an inverse MC scheme to recover the reduced scattering coefficients of both the layers and the total hemoglobin (Hb) concentration of the bottom layer. It was reported that the data procured by the beveled probe recovered the reduced scattering coefficient of the top layer more accurately as compared to the perpendicular probe. The spot size of incident light on the tissue was 350  $\mu\text{m}$ , which limited the minimum SDS to 0.4 mm in the oblique probe. Reducing the minimum SDS further can recover the properties of the superficial layer even more accurately.

There have been in-vivo studies to extract the optical properties of cervical tissue based on SRR using fiber optic probes [16,17]. Chang et al. [16] and Hornung et al. [17] could not extract optical properties of the superficial layer due to limitations of their probe geometries. To the best of our knowledge, the existing probes for epithelial cancer diagnosis have not been able to provide accurate optical properties of epithelium layer and its variation with the progression of pre-cancer. Hence, there is a need to develop an SRR based probe to acquire signals majorly from epithelium, aiding early-stage diagnosis of epithelium cancer. Choice of appropriate inverse scheme is crucial for accurate recovery of the optical parameters. These schemes typically thrive on the accuracy of the forward solver that generates the synthetic SRR at desired detector locations. The analytical solutions to

diffusion approximated radiative transport equation (DA-RTE) have been used for estimation of optical parameters of diffusive media [8,9,18], for large SDSs. However, for small SDSs as well as for low-scattering media, photons get collected at the detectors before they are completely diffused, and hence it is erroneous to employ DA-RTE to model reflectance for such cases [19]. An MC method is a numerical equivalent to solve the RTE which is the analytical model for simulating accurate light transport in tissue. Therefore a variety of MC based reconstruction schemes such as empirical model [20,21], MC fast and flexible inverse model [22,23], perturbation MC model [24], scalable MC model [4,22,23,25], MC look-up table (MC-LUT) based schemes [26–30], artificial neural network method [31] have been extensively used for estimation of optical properties of turbid media. Based on these studies, we have focused on: (1) a MC-based detailed comparative study of the efficacy of common probe-geometries for epithelial precancer diagnosis, and (2) accurate recovery of optical parameters of the top layer from SRR data collected by a novel fiber-optic probe using MC look-up table (MC-LUT) based inversion.

This manuscript is organized as follows: Section 2 provides a brief theory of light propagation in turbid media and discusses the basic inverse problems involved. In Section 3 we study the efficacy of various probe geometries for epithelial precancer diagnosis. Section 4 provides the details of the fabricated fiber-optic probe, experimental set-up for accurate SRR collection and MC-LUT based extraction of optical parameters, and the results thus obtained are discussed in Section 5. The concluding remarks are offered in Section 6.

## 2. Background Theory

During changes occurring in the development of epithelial precancer, physiological and structural changes in tissue are primarily reflected in the optical parameters (absorption and scattering coefficients) of the top (epithelial) layer. Typically the epithelium layer is very thin ( $\sim 200\text{--}500\text{ }\mu\text{m}$ ), and hence in order to probe signatures of epithelial perturbations collection of photons close to the source is desirable. In order to recover the optical parameters of the epithelium layer, a mathematical model to simulate photon propagation accurately in the vicinity of the source is imperative.

### 2.1. Radiative Transfer Equation

The radiative transport equation (RTE) [32,33] is the globally accepted analytical model to simulate accurate photon propagation in biological tissues. In steady state, the RTE is given as,

$$(\hat{n} \cdot \nabla + \mu_a(\vec{x}) + \mu_s(\vec{x})) I(\vec{x}, \hat{n}) - \mu_s(\vec{x}) \int_{S^2} I(\vec{x}, \hat{n}') P(\hat{n}, \hat{n}') d\omega' = q(\vec{x}, \hat{n}), \quad (1)$$

where  $\nabla$  is the gradient operator,  $\mu_a$  and  $\mu_s$  are absorption and scattering coefficients of the medium,  $I(\vec{x}, \hat{n})$  is the radiance at a position  $\vec{x}$  inside the medium in  $\hat{n}$  direction, and  $q(\vec{x}, \hat{n})$  represents the source term. The phase function  $P(\hat{n}, \hat{n}')$  is the probability density function governing the scattering of a beam incident from  $\hat{n}$  into  $\hat{n}'$  direction. For this work, we have utilized the commonly used “Heney–Greenstein phase function” [33].

$$P(\hat{n}, \hat{n}') = \frac{1}{2^{n-1}\pi} \frac{1 - g^2}{(1 + g^2 - 2g(\hat{n}, \hat{n}'))^{d/2}} \quad (2)$$

where  $g$  is known as the anisotropy factor, mathematically defined as  $\langle \hat{n} \cdot \hat{n}' \rangle$  and  $d$  takes the values 2 and 3 for 2D and 3D RTE respectively.

The RTE is an integro-differential equation and solving it numerically is mathematically challenging as well as computationally expensive. Typically, the tissue is dominantly a scattering medium where RTE reduces to the diffusion equation [33], a partial differential equation, much easier to solve as compared to RTE. However, to investigate superficial regions such as the epithelium

from where light captured does not go through large scattering events, RTE is more appropriate. A numerical equivalent of solving the RTE is the MC simulation [33,34].

## 2.2. Recovery of Optical Parameters

Characteristic optical properties of tissue are encoded in the boundary optical measurements (SRR data). A typical optical inverse problem is to reconstruct from a set of SRR measurements, the spatial distributions of the underlying optical parameters such as  $\mu_a, \mu_s, g$  etc. that produced them, i.e., the unknown parameters in the map:

$$\Lambda_{\mu_a, \mu_s, g} : S_x(\vec{r}) \mapsto \mathcal{R}_{meas}(\vec{r}_d)_{|\{\vec{r}_{d_1} \dots \vec{r}_{d_M}\}} \quad (3)$$

where  $S_x(\vec{r})$  denotes the excitation source and  $\mathcal{R}_{meas}(\vec{r}_d)_{|\{\vec{r}_{d_1} \dots \vec{r}_{d_M}\}}$  represents the SRR measurements at  $M$  detectors. Over the past three decades, various optical inverse problems have been extensively explored. These problems are non-linear in nature and typically solved using non-linear optimization techniques. There is a plethora of research work involving the point-wise reconstruction of optical parameters using RTE [35–40] as well as DA-RTE [41–46]. These techniques are computationally expensive and need a lot of time to reconstruct the maps of desired optical parameters. Moreover, such techniques also demand a huge amount of experimental data, which is impractical when probing internal organs since the site available for observation would usually have a small area.

Optical parameters recovered from the epithelial and stromal layers have been known to reflect changes due to carcinoma [4,15,25–27,47,48]. However, with point-wise reconstruction, there is a high probability of missing valuable information from this layered structure. Instead, their layer-wise extraction would be more efficient and accurate. This reduces the number of unknowns tremendously and consequently the small number of measurements would yield accurate recovery of the optical parameters.

For our work, we have utilized a MC-LUT based scheme [26–30] to extract the optical parameters of the phantoms. Multilayered MC program [34] has been used to generate synthetic SRR data at detectors. The synthetic SRR data obtained by varying an optical parameter are tabulated into a two dimensional matrix (known as the MC-LUT). For recovery of a set of unknown optical parameters, the experimental SRR values are compared with the MC look-up table and the minimizer of the root-mean-square-error is the reconstructed set of optical parameters.

## 3. Potential of Various Probe Designs for Epithelial Precancer Diagnosis

A MC simulation based analysis has been performed to study the efficacy of various fiber-optic configurations to capture changes occurring in the epithelium.

### 3.1. Modifications in MC Simulation

We modified the multilayer MC code developed by Wang et al. in 1995 [34], incorporating a few changes in order to suit our requirements. Reflectance and internal fluence were stored in voxels instead of annular rings or shells. While launching and collecting the photons, the numerical aperture (NA) as well as the contact area of the optical fibers were taken under consideration due to the short SDS used. The launching and collection of photons were also modeled for beveled tip fibers as per [49].

The medium was discretized into cubic voxels of sidelength  $10 \mu\text{m}$ . The light was launched randomly from positions inside the ellipse with major axis  $50\sqrt{2} \mu\text{m}$  and minor axis  $50 \mu\text{m}$  with equal probability. The axis of fiber was at  $\beta = 45^\circ$  with respect to the normal of the surface. If the refractive index of the fiber core and tissue were  $n_1 = 1.47$  and  $n_2 = 1.35$  respectively, the light exiting the fiber would be refracted by an angle  $\gamma \approx 5^\circ$  [49]. So, direction cosines of the incident photons were randomized uniformly within the cone of NA of the fiber along the refraction angle. The weights of photons emitted from the surface within the NA of detection fibers were stored in corresponding square surface bins of side length  $10 \mu\text{m}$ .

We also computed the quantity “Epithelial Sensitivity” ( $\mathcal{E}$ ) at a detector position, which is defined as the ratio of the integrated weights of photons, which ejected out of the phantom surface at the detector location without entering the stromal layer to the total weight of photons collected at that detector. It serves as an indicator of the ability of a detector location to reveal subtle changes in the epithelium layer and hence the potential to diagnose epithelial pre-cancer.

### 3.2. Effect of Orientation of Fibers

In this section, we study the effect of the orientation of optical fibers on the epithelium sensitivity. Using the Monte Carlo simulations it has been established [12] that change in the bevel angle of the source as well as collection fibers not only affects the amount of the collected photons but also governs the depth selection. To verify the effect of the bevel angle of the collection fiber on the depth sensitivity, MC simulations have been performed for a two layered phantom irradiated by a fiber oriented normal to the phantom. The spatially resolved epithelial sensitivity for multiple bevel angles ( $10^\circ, 30^\circ, 50^\circ, 70^\circ$ ) of the collection fibers (Figure 1a) were obtained from the simulations and demonstrated in Figure 1b. As expected, increased bevel angle of the collection fibers was observed to yield better epithelial sensitivity. We further evaluated three probe geometries, commonly found in the literature [11,15]: Probe geometry-I: unbeveled source and detector fibers placed normal to the phantom surface (Figure 2a). Probe geometry-II: beveled source and detector fibers (bevel angle  $\beta = 45^\circ$ ) on the phantom surface (Figure 2b). Probe geometry-III: beveled source and detector fibers (bevel angle  $\beta = 45^\circ$ ) with the source and detector fibers oriented in opposite directions as shown in Figure 2c. While the probe geometry-I has already been thoroughly studied in [4,6,8,9,16], we have included it in our analysis for completeness.

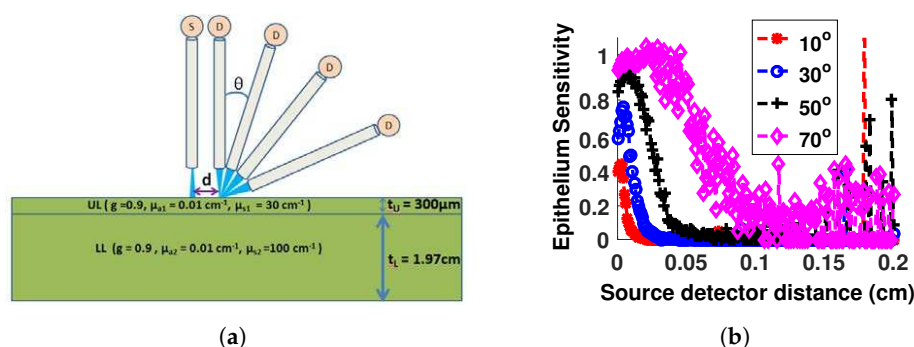


**Figure 1.** (a) Source-detector geometry in which detector fibers are at  $10^\circ, 30^\circ, 50^\circ, 70^\circ$  bevel angles, (b) variation of epithelium sensitivity with bevel angles and source-detector distances, plot with red curve shows spatially resolved epithelium sensitivity at a  $10^\circ$  bevel angle and similarly, blue, black and magenta curves represent epithelium sensitivity at  $30^\circ, 50^\circ$ , and  $70^\circ$  bevel angles respectively (color online only).

Figure 2d–f depicts the 2-d spatial distribution of reflectance obtained from the MC simulations for the three probe geometries. The asymmetry in the collected SRR as observed in Figure 2e,f is due to asymmetry in the source-detector configurations in probe geometry-II and III respectively. The plot of  $\mathcal{E}$  along the x- and y- axes are depicted in Figure 2g–i.

The most commonly used probe geometry (I) has a sharp drop in  $\mathcal{E}$  along both axes (Figure 2g). The probe geometry-II, with the beveled source and detection fibers, shows substantially improved  $\mathcal{E}$  along x-axis (Figure 2h). The best epithelial the sensitivity is obtained with probe geometry-III (Figure 2i), where significant values of  $\mathcal{E}$  are observed upto 1 mm. The numerical analysis shows that the probe-geometry III is the most suitable for epithelial pre-cancer detection. While for internal organs it is not feasible to employ such a geometry, it can be used for early detection of cancer in the external organs such as skin and oral cavity. Hence, in our study we have utilized probe geometry-II.



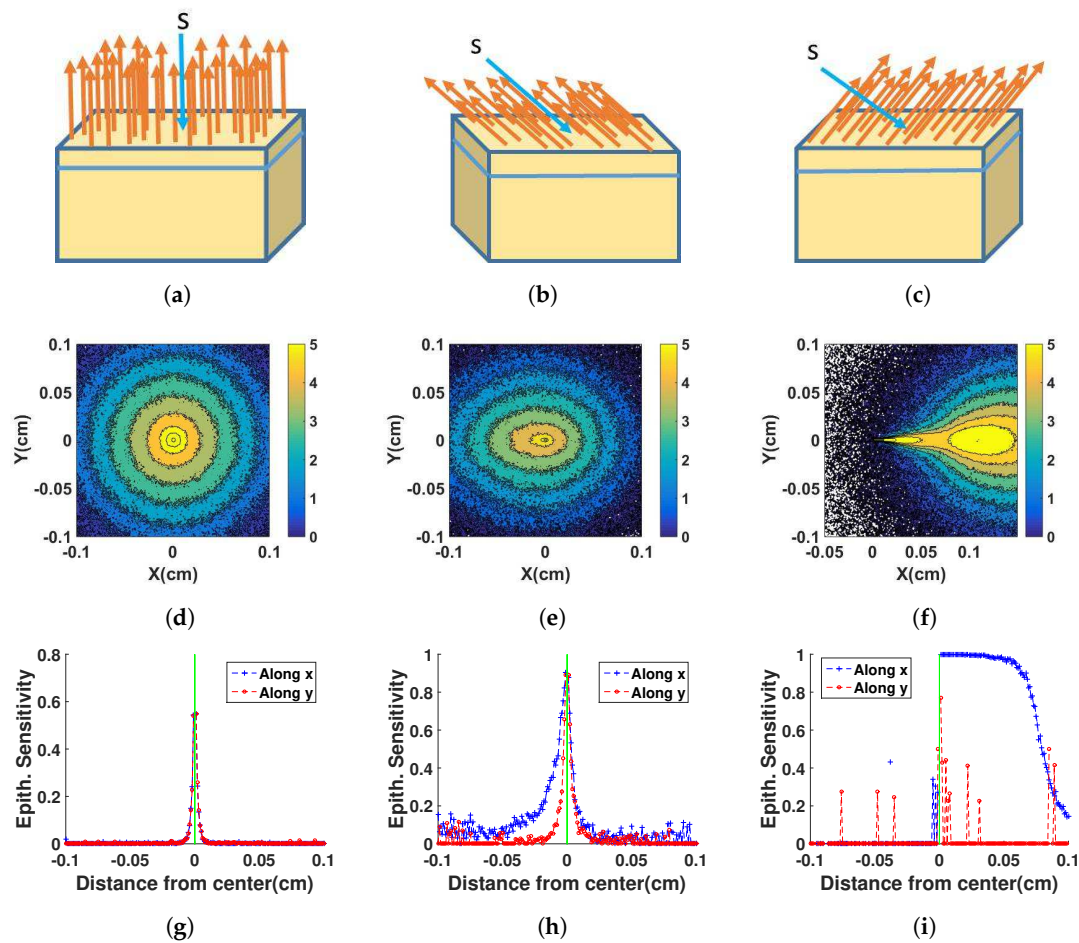


**Figure 2.** probe geometry-(a) I, (b) II, and (c) III. In each of the three geometries, the blue arrow shows the launching direction of photon and orange arrows indicates the axis of collection of photons for SRR measurement. (d–f) show the 2-dimensional collection of SRR, and (g–i) show the epithelial sensitivities along the x-axis and y-axis for probe geometries-I, II, and III respectively. Width of the green region at the center of each of the plots (g–i) indicates the size of the source (color online only).

### 3.3. Effect of Diameter of Launching Optical Fibers

In this section we describe the effects of source fiber diameter on sensitivity of the probe to diagnose epithelial precancer. We varied the diameter of the source fiber (50, 100 and 200  $\mu\text{m}$ ) in the probe geometry-II and Figure 3 demonstrates the corresponding SRR and  $\mathcal{E}$ . Increase in diameter of the launching fiber not only limits the minimum SDS, but also leads to decrements in  $\mathcal{E}$  values. Therefore a fiber optic probe with thin source fiber is desirable for early diagnosis of the disease.

### 3.4. Effect of Bevel Angle of Optical Fibers

Figure 4 depicts the variation of SRR and  $\mathcal{E}$  for three bevel angles ( $30^\circ$ ,  $45^\circ$ ,  $60^\circ$ ) of the fibers in the endoscopic probe geometry-II. While the increasing bevel angle was found to improve the epithelial sensitivity (Figure 4d–f), the SRR strength was better at a lower bevel angle. Therefore,  $45^\circ$  can be chosen as the optimal bevel angle for an endoscopic probe aiming at epithelial precancer diagnosis.

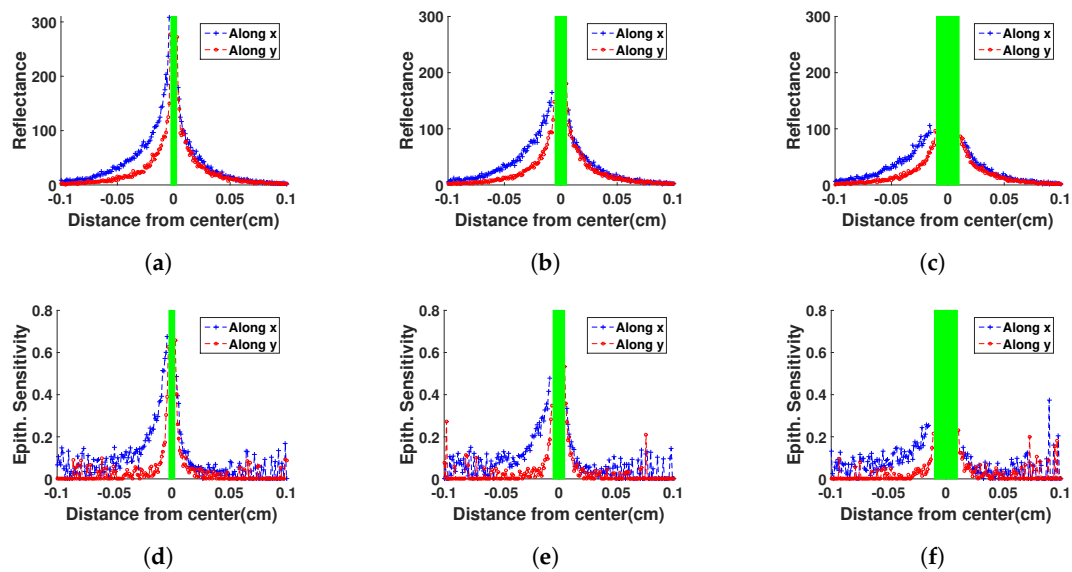


**Figure 3.** For probe geometry-II and bevel angle  $\beta = 45^\circ$ , the collected SRR along x- and y- axes for source fiber diameters (a) 50  $\mu\text{m}$ , (b) 100  $\mu\text{m}$ , and (c) 200  $\mu\text{m}$ . Corresponding epithelial sensitivity plots for source fiber diameters (d) 50  $\mu\text{m}$ , (e) 100  $\mu\text{m}$ , and (f) 200  $\mu\text{m}$ . Width of the green region at the center of each of the plots indicates the size of the source (color online only).

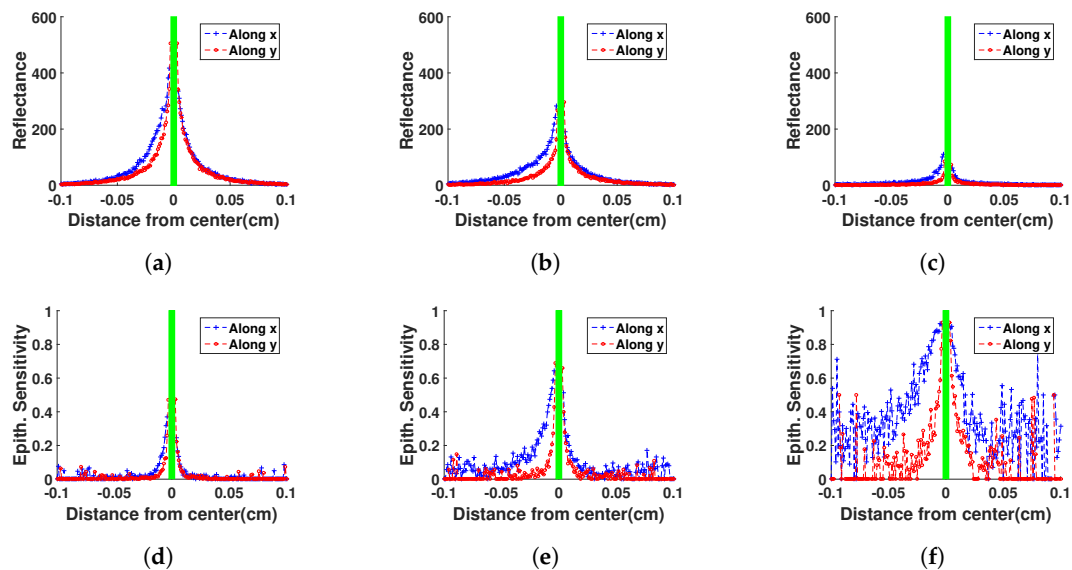


**Figure 4.** For probe geometry-II and source fiber diameter 50  $\mu\text{m}$ , the collected SRR along x- and y- axes for bevel angles (a)  $\beta = 30^\circ$ , (b)  $\beta = 45^\circ$ , and (c)  $\beta = 60^\circ$ . Corresponding epithelial sensitivity plots for bevel angles (d)  $\beta = 30^\circ$ , (e)  $\beta = 45^\circ$ , and (f)  $\beta = 60^\circ$ . Width of the green region at the center of each of the plots indicates the size of the source (color online only).

## 4. Materials and Methods

### 4.1. Preparation of Two Layered Phantoms

An epithelial tissue-mimicking phantom was prepared with scatterers, absorbers and a medium to hold these optically interactive agents homogeneously. Nigrosin dye was chosen as the absorber, and Intralipid-20 (IL-20) was used as the scatterer which is commonly used for UV-visible region of light. The concentrations of the absorber and scatterer can be chosen to prepare phantoms with desired optical properties. An epithelial tissue-mimicking phantom was prepared with a 300  $\mu\text{m}$  thin

superficial layer mimicking the epithelium, and the bottom layer mimicking stroma was chosen to be 1.97 cm thick.

Two optical phantoms were with optical properties: (1)  $\mu_a$  (top) = 2 cm<sup>-1</sup>,  $\mu_s$  (top) = 40 cm<sup>-1</sup>,  $\mu_a$  (bottom) = 4.3 cm<sup>-1</sup>,  $\mu_s$  (bottom) = 250 cm<sup>-1</sup>, (2)  $\mu_a$  (top) = 2.5 cm<sup>-1</sup>,  $\mu_s$  (top) = 55 cm<sup>-1</sup>,  $\mu_a$  (bottom) = 4.3 cm<sup>-1</sup>,  $\mu_s$  (bottom) = 250 cm<sup>-1</sup> mimicking normal and precancerous cervical tissue, respectively [50].

## 4.2. Instrumentation

### 4.2.1. Proposed Design of Probe and Fabricated Prototype

Based on the simulation results presented in the previous Sections 3.2–3.4, a probe as depicted in Figure 5a was designed for the diagnosis of cervical precancer. Figure 5b displays the design of the tip of the probe which consists of two concentric stainless steel tubes. Inner tube with inner and outer diameters of 340 and 410  $\mu$ m respectively contains 19 fibers of diameter 50/65  $\mu$ m. The outer tube has 1.16 mm inner and 5 mm outer diameter and it contains the first tube at the center and 58 fibers of diameter 100/125  $\mu$ m between the vacant space. The proximal end of the probe is a stainless steel cylindrical body (diameter 5 mm and length 15 cm) containing fibers. All the fibers at the proximal end of the probe are polished at 45° (the bevel angle) with respect to the axis of the cylinder. At the distal end, these fibers are bifurcated and can be connected to the detectors or the source individually.

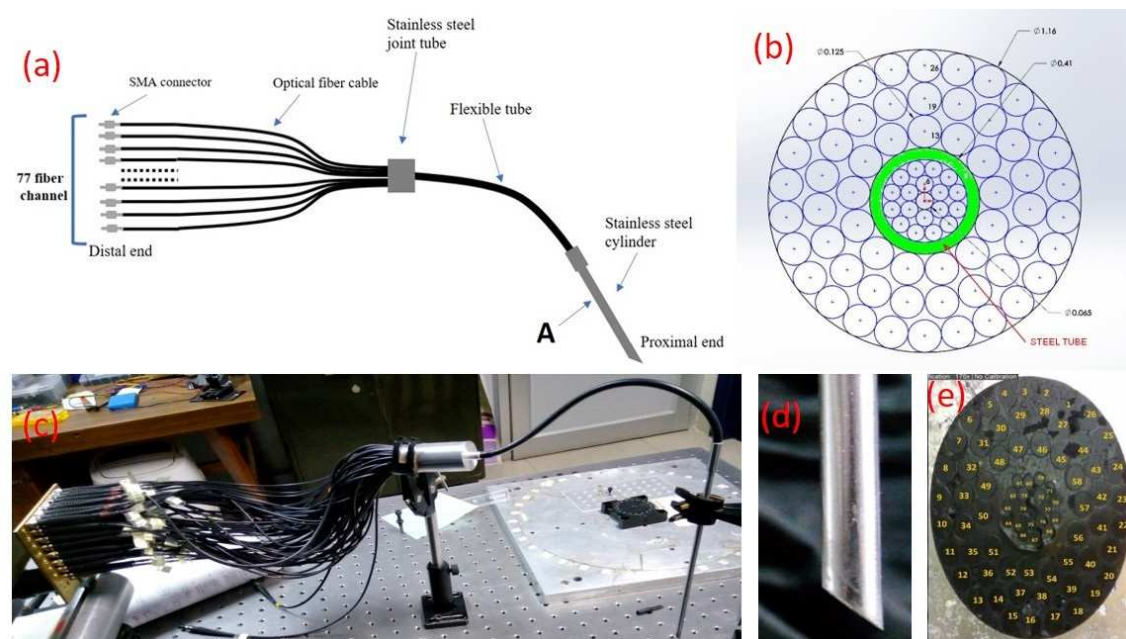


**Figure 5.** (a) Schematic diagram of designed probe, (b) perpendicular cross section of probe near proximal end as per the proposed design, (c) fabricated prototype of the probe, (d) beveled tip of the probe at proximal end, (e) arrangement of fibers on the tip of probe at proximal end (after fabrication)

The proposed probe was fabricated at FiberTechOptica, Ontario, Canada and is shown in Figure 5c. The beveled proximal end and the tip of the probe are depicted in Figure 5d,e respectively. Because of manufacturing limitations, the fabricated prototype of the probe does not have the symmetric arrangement of the inner ring fibers as proposed in the design (Figure 5b).

### 4.2.2. Experimental Set-up

The schematic diagram and photograph of the steady-state SRR measurement set-up is demonstrated in Figure 6.



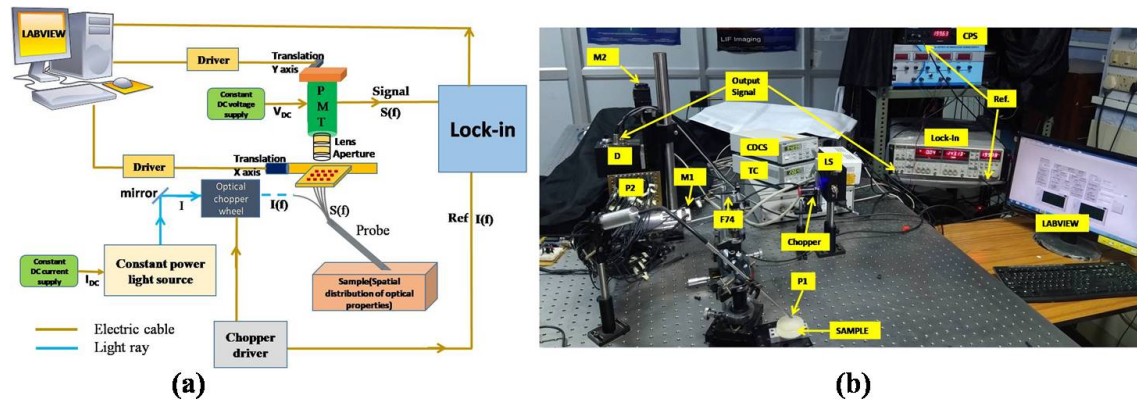


**Figure 6.** (a) Schematic diagram, and (b) photograph of experimental set-up used to collect steady state spatially resolved reflectance; LS—Light Source, P—Probe, D—Detector, CDCS—Constant DC current supply, TC—temperature controller, P1—Proximal end of probe, P2—Distal end of probe, M1 and M2 are stepper motors connected for x-axis and y-axis translation, CPS—Chopper power supply, F74—fiber number 74 in Figure 5e used as source fiber.

The set-up consists of three major parts: a light source (LS), a probe (P) and a light detection system (D). Here the light source (LS) provides a laser light of center wavelength 450 nm. This light source includes a PL450B (THORLABS) laser diode on a mount connected to a constant DC current supply to drive the diode and a temperature controller. The laser diode emits constant power output which is chopped at 200 Hz by a chopper. The probe (P) is used to deliver the light from the light source to the surface of the sample and transmit the collected backscattered light at different spatial locations on the surface of the sample to the detector (D). The design and arrangement of fibers in the probe is explained in Section 4.2.1. The proximal end (P1) of the probe is kept onto the surface of the sample. One of the fibers (Fiber number 74 in Figure 5e), approximately at the center of the proximal end (P1) is coupled to the chopped the light source to irradiate the sample. Distal ends (P2) of remaining fibers are connected to a brass plate, which is mounted on an x-axis translation stage connected to a stepper motor (M1). Light coming out from the distal end of each fiber (except fiber number 74) is collected by a photomultiplier tube (PMT) (Hamamatsu R928), which is also mounted on a y-axis translation stage through another stepper motor M2. The relative motions of the x-axis and y-axis translation stages couple light sequentially from each of the fibers to PMT. The signal from PMT is fed to a lock in-amplifier (Model no: SRS-830). A reference signal obtained from the chopper power supply is also fed to the lock-in amplifier. The stepper motors (M1 and M2), as well as the lock-in amplifier are interfaced to the computer and a LABVIEW based program has been developed to automate the entire system and collect signal from each of the output fibers.

#### 4.3. Validation of Measured Reflectance and Epithelial Sensitivity with Simulated Results

The probe was calibrated for uniform illumination by storing the intensity value of each fiber. Inverse of this intensity value was saved as a correction factor of each fiber of the probe. A homogenous intralipid solution of scattering coefficient  $\mu_s = 100 \text{ cm}^{-1}$  was irradiated using source fiber (fiber number 74 in Figure 5e) and reflectance was measured from each of the fibers. The reflectance measured from each fiber was multiplied by the calibration factor to obtain a corrected spatially resolved reflectance pattern. The measured corrected spatially resolved reflectance was compared with the modified MC (Section 3.1) simulated data and shown in Figure 7a,b for fiber numbers 1 to 58 except 24, 25, 26 and 40 (these fibers were not connected to light detection system due to lack of collection efficiency).

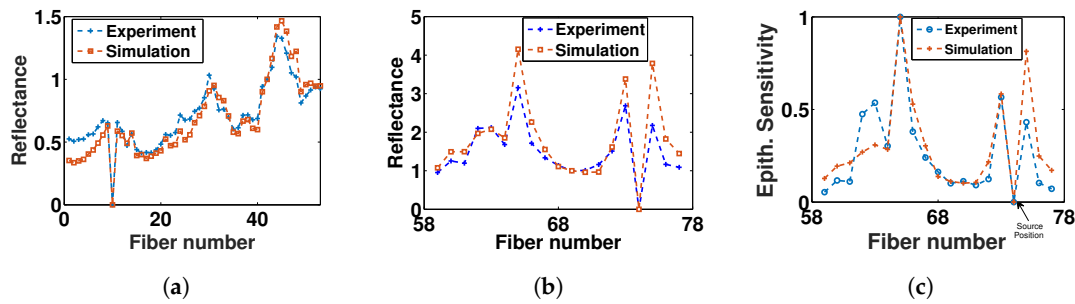


**Figure 7.** Comparison of simulated data and experimental data (a) for 53 outer ring fibers from 1 to 58 (measurement was not taken for fibers 24, 25, 26, 40 and 46) and (b) for all fibers of inner ring from 59 to 77, and (c) epithelial sensitivity measurement for inner ring fibers.

For epithelial sensitivity measurement, SRR was measured from a two-layered phantom prepared with a highly absorbing ( $\mu_a = 100 \text{ cm}^{-1}$ ) and minimally scattering ( $\mu_s = 0.001 \text{ cm}^{-1}$ ) bottom layer, and the optical properties of the top layer were chosen as  $\mu_a = 2.5 \text{ cm}^{-1}$ ,  $\mu_s = 40 \text{ cm}^{-1}$  and thickness of top layer =  $300 \text{ }\mu\text{m}$ . The reflectance from each fiber was experimentally measured and corrected. The highly absorbing and minimally scattering bottom layer ensures that the photons which once enter the bottom layer have a negligible probability of exiting to the top layer and contribute to the SRR. Therefore, the measured SRR for such a phantom is an indicator of the epithelial sensitivity. Numerical SRR data was generated for a phantom with the same optical properties as the aforementioned two-layer phantom using the modified MC code. The experimentally measured and numerically computed epithelial sensitivity for fibers 59 to 77 are plotted in Figure 7c indicating good agreement between the experiment and the simulation. The other fibers collect photons traveling majorly in bottom layer which were absorbed and so the reflectance values on fiber numbers 1 to 58 were very low. These did not match with the simulated data primarily due to low SNR.

#### 4.4. Schemes for Recovery of Optical Parameters

##### 4.4.1. Generation of MC Look-Up Table

Modified MCML (Section 3.1) program was executed to simulate the SRR as well as the epithelial sensitivity at each of the 76 detector fibers for a set of fixed (known) and free (unknown) optical parameter values. The term ‘free’ refers to the parameters which we aim to reconstruct. In this study the goal is to extract the optical parameters of the epithelium layer and hence the scattering and absorption coefficients of the top layer are considered as the free optical parameters. The values of free parameters for which the simulations are executed are chosen a priori, based on our knowledge of the range of the optical parameters for the tissue to be probed.

We tabulated the synthetic SRR data for top layer absorption coefficients:  $\mu_a^t = 1, 3, 5, 7$  and  $9 \text{ cm}^{-1}$  and scattering coefficients:  $\mu_s^t = 20, 40, 60, 80$ , and  $100 \text{ cm}^{-1}$ . We further generated SRR data for absorption coefficients:  $1\text{--}9 \text{ cm}^{-1}$  in steps of  $0.05 \text{ cm}^{-1}$  and scattering coefficient:  $20\text{--}100 \text{ cm}^{-1}$  in steps of  $1 \text{ cm}^{-1}$  using cubic interpolation. This process builds the three-dimensional MC-LUT of size  $(76 \times 161 \times 81)$ .

##### 4.4.2. Extraction of Free Optical Parameters

The inversion scheme minimizes the error between the synthetic SRR tabulated in MC-LUT and the measured SRR from the unknown sample, and the minimizer thus obtained is the extracted optical parameter of interest.

**Problem-I:** The first minimization problem we solve is to recover the absorption coefficient of the top layer  $\mu_a^t$ , if the top layer scattering coefficient  $\tilde{\mu}_s^t$ , and both the optical parameters of the bottom layer ( $\tilde{\mu}_a^b, \tilde{\mu}_s^b$ ) are known, that is

$$\hat{\mu}_a^t = \arg \min_{\mu_a^t} \epsilon(\mu_a^t) = \|\underline{R}^{meas} - \underline{R}^{pred}(\mu_a^t, \tilde{\mu}_s^t, \tilde{\mu}_a^b, \tilde{\mu}_s^b)\|_2^2 \quad (4)$$

where  $\underline{R}^{meas} = (R_1^{meas}, R_2^{meas}, \dots, R_N^{meas})$ , and  $\underline{R}^{pred} = (R_1^{pred}, R_2^{pred}, \dots, R_N^{pred})$  represent the measured and predicted SRR values, respectively, at  $N$  detection fibers. While carrying out numerical validations (Section 5.1),  $\underline{R}^{meas}$  refers to synthetic SRR measurements from the sample with unknown optical properties and in case of experimental studies (Section 5.2) it refers to the experimentally measured SRR.

**Problem-II:** Next, we aim to recover the scattering coefficient of the top layer  $\mu_s^t$ , given the top layer absorption coefficient  $\tilde{\mu}_a^t$  and both the optical parameters of the bottom layer ( $\tilde{\mu}_a^b, \tilde{\mu}_s^b$ ), by solving the minimization problem:

$$\hat{\mu}_s^t = \arg \min_{\mu_s^t} \epsilon(\mu_s^t) = \|\underline{R}^{meas} - \underline{R}^{pred}(\tilde{\mu}_a^t, \mu_s^t, \tilde{\mu}_a^b, \tilde{\mu}_s^b)\|_2^2 \quad (5)$$

**Problem-III:** In order to recover both the optical parameters of the top layer ( $\mu_a^t, \mu_s^t$ ) for known optical parameters of the bottom layer ( $\tilde{\mu}_a^b, \tilde{\mu}_s^b$ ), the following minimization problem needs to be solved:

$$\hat{\mu}_a^t, \hat{\mu}_s^t = \arg \min_{\mu_a^t, \mu_s^t} \epsilon(\mu_a^t, \mu_s^t) = \|\underline{R}^{meas} - \underline{R}^{pred}(\mu_a^t, \mu_s^t, \tilde{\mu}_a^b, \tilde{\mu}_s^b)\|_2^2 \quad (6)$$

## 5. Results and Discussion

We carried out a detailed step-by-step analysis to study the potential of the fabricated probe to recover the optical parameters of a two-layered numerical phantom from numerical as well as experimental data.

### 5.1. Numerical Studies

The modified MC simulations (Section 3.1) were executed for two-layered numerical media for the desired optical parameters and SRR was extracted from the locations which mimic the positions of detection fibers of the probe. The synthetic SRR data was then contaminated with 5% Gaussian noise. The data thus procured, mimics the experimental SRR measurement collected by the fabricated probe.

#### 5.1.1. Recovery of the Absorption Coefficient of the Top Layer

We first considered Problem-I mentioned in Section 4.4.2. The absorption and scattering coefficients of the bottom layer were fixed at  $4.3 \text{ cm}^{-1}$  and  $250 \text{ cm}^{-1}$ . The scattering coefficient of the top layer was chosen to be  $40 \text{ cm}^{-1}$ , and the values of true and extracted absorption coefficients, obtained by solving Equation (4) are tabulated in Table 1.

**Table 1.** Reconstruction of absorption coefficient of the top layer from simulated data with prior knowledge of scattering coefficient of top layer and both optical properties of bottom layer (Problem-I).

Phantom ID	True Value $\mu_a \text{ (cm}^{-1}\text{)}$	Extracted Value $\mu_a \text{ (cm}^{-1}\text{)}$	Std. Deviation $\text{(cm}^{-1}\text{)}$
1	2.0	1.9	0.1
2	2.5	2.4	0.1
3	4.0	4.0	0.2
4	6.0	6.0	0.2
5	8.0	8.0	0.2

### 5.1.2. Reconstruction of Only Scattering Coefficient of Top Layer

We now solved Problem-II mentioned in Section 4.4.2. The absorption and scattering coefficients of the bottom layer were fixed at  $4.3 \text{ cm}^{-1}$  and  $250 \text{ cm}^{-1}$ . The absorption coefficient of the top layer was chosen to be  $3 \text{ cm}^{-1}$ , and the values of true and extracted scattering coefficients, obtained by solving Equation (5) are tabulated in Table 2.

**Table 2.** Reconstruction of scattering coefficient of top layer from simulated data with prior knowledge of absorption coefficient of top layer and both optical properties of bottom layer (Problem-II).

Phantom ID	True Value $\mu_s (\text{cm}^{-1})$	Extracted Value $\mu_s (\text{cm}^{-1})$	Std. Deviation ( $\text{cm}^{-1}$ )
1	30	31	3
2	50	51	2
3	70	69	2
4	90	91	2

### 5.1.3. Simultaneous Reconstruction of Absorption and Scattering Coefficient of Top Layer

We then implemented the MC-LUT based optimization to solve Problem-III mentioned in Section 4.4.2. Synthetic SRR data were generated using MC simulation for two-layered numerical phantoms. The absorption and scattering coefficients of the bottom layer were fixed at  $4.3 \text{ cm}^{-1}$  and  $250 \text{ cm}^{-1}$ . The true and recovered values of the optical parameters of the top layer, obtained by solving Equation (6) are tabulated in Table 3.

**Table 3.** Simultaneous reconstruction of absorption and scattering coefficients of the top layer from simulated data with prior knowledge of both the optical properties of bottom layer.

Phantom	True Value ( $\text{cm}^{-1}$ )		Extracted Value ( $\text{cm}^{-1}$ )		Std. Deviation ( $\text{cm}^{-1}$ )	
	$\mu_a$	$\mu_s$	$\mu_a$	$\mu_s$	$\delta\mu_a$	$\delta\mu_s$
1	5.2	72	5.4	74	0.1	2
2	1.7	72	1.6	69	0.2	3
3	5.2	32	5.4	36	0.1	4

It is well established that the optical parameters of the bottom layer can be recovered with little error [4,15,25–27,31,47,48]. Therefore, we carried out the recovery of the top layer optical parameters, when the optical parameters of the bottom layer are known with  $\sim 10\%$  error and the results thus obtained are tabulated in Table 4. The first two columns of Table 4 consist of the true values of the optical parameters of the numerical phantoms. However, the MC-LUT used for extraction of top layer optical parameters correspond to the bottom layer optical parameters  $\mu_a = 4.3 \text{ cm}^{-1}$  and  $\mu_s = 250 \text{ cm}^{-1}$ . We observed that the inaccuracy in the optical properties of the bottom layer affects the accuracy of the recovered top layer absorption coefficient ( $\sim 20\%$  error). However, the top layer scattering coefficient is still recovered accurately ( $< 6\%$  error).

**Table 4.** Simultaneous recovery of absorption and scattering coefficients of the top layer from simulated data, when the bottom layer optical parameters are known with  $\sim 10\%$  error.

Phantom	True Value (Top Layer) ( $\text{cm}^{-1}$ )		True Value (Bottom Layer) ( $\text{cm}^{-1}$ )		Extracted Value (Top Layer) ( $\text{cm}^{-1}$ )		Std. Deviation ( $\text{cm}^{-1}$ )	
	$\mu_a$	$\mu_s$	$\mu_a$	$\mu_s$	$\mu_a$	$\mu_s$	$\delta\mu_a$	$\delta\mu_s$
1	5.2	72	3.8	225	6.0	73	0.3	2
2	5.2	72	3.8	275	6.2	74	0.2	2
3	5.2	72	4.8	225	6.1	74	0.3	2
4	5.2	72	4.8	275	5.9	73	0.3	2

## 5.2. Experimental Studies

We prepared two phantoms; one mimicking a normal and the other mimicking a pre-cancerous cervical tissue. The fiber optic probe (probe-geometry II) was employed to measure the SRR. We performed the simultaneous recovery of optical parameters of the top layer from the experimental SRR data procured using the probe. Details of the probe, phantom preparation, and the experimental setup have already been described in Section 4. The choice of optical parameters of the cervical tissue-mimicking phantoms was based on [12,50]. The algorithm proposed to solve Equation (6) was numerically validated in Section 5.1.3 and was implemented on the experimental data to recover the absorption and scattering coefficients of the top layer simultaneously. The results thus obtained are tabulated in Table 5. The algorithm was able to extract the absorption and scattering coefficients of the top layer with a maximum of 6.7% and 3.3% errors  $\text{Error} = \frac{\text{TrueValue} - \text{RecoveredValue}}{\text{TrueValue}} \times 100$ ), respectively, as compared to their true values.

**Table 5.** Simultaneous reconstruction of absorption and scattering coefficients of the top layer from experimental SRR data with prior knowledge of both the optical properties of bottom layer.

Phantom	True Value ( $\text{cm}^{-1}$ )		Extracted Value ( $\text{cm}^{-1}$ )		Std. Deviation ( $\text{cm}^{-1}$ )		Error (%)	
	$\mu_a$	$\mu_s$	$\mu_a$	$\mu_s$	$\delta\mu_a$	$\delta\mu_s$	$\epsilon\mu_a$	$\epsilon\mu_s$
1	3.0	60	3.2	58	0.2	2	6.7	3.3
2	2.5	80	2.4	82	0.3	3	4	2.5

## 6. Conclusions

In the early stages of epithelial cancer, changes occur in the structure and biochemistry of 200–500  $\mu\text{m}$  thick epithelium layer. In this paper, we carry out a detailed numerical evaluation of various probe geometries for early diagnosis of epithelial pre-cancer based on spatially resolved reflectance. It was concluded that a parallel-oblique fiber-optic probe, beveled at  $\beta = 45^\circ$ , and with minimal source detector distance is an appropriate choice. The fiber-optic probe was accordingly fabricated. The experimental SRR and epithelial sensitivity measurements for test phantoms were performed and were found in good agreement with computational data. Synthetic SRR data was generated by MC code for two-layered epithelial tissue phantoms, and contaminated with 5% Gaussian noise. Optical parameters of the top layer were accurately recovered using a MC-look up table based inversion scheme. To further check the efficacy of the algorithm, the top layer optical parameters were extracted from the SRR data, using the MC-LUT, when there was  $\sim 10\%$  error in the recovered optical parameters of the bottom layer. The top layer absorption coefficient thus recovered was found to be off by  $\sim 20\%$  of its true value, while the scattering coefficient was recovered quite accurately with a  $< 6\%$  error (Table 4). After the scheme of simultaneous recovery of absorption and scattering coefficients of top layer was numerically validated, it was further employed on experimental SRR measurements obtained using the fabricated probe from epithelial tissue-mimicking two-layered



phantoms. The top layer optical parameters were accurately recovered with absorption and scattering coefficients extracted within 6.7% and 3.3% of their respective true values.

The top layer optical properties were reconstructed by measuring only spatially resolved reflectance measurements at a single wavelength (450 nm). The other methods, reported in [15,50] use white-light source and spectrometer to collect spectral reflectance to extract optical properties of the superficial layer of the phantom. In comparison to other methods the proposed probe in combination with the laser source and light detector renders to be more accurate and sensitive for the epithelial layer's discriminative signatures, and hence, has the potential to be a competent tool for the diagnosis of cervical cancer at early stages. The developed system can be further improved for fast reconstruction by using only some fibers with higher epithelial sensitivity. The spectral measurements with this probe can extract more features related to superficial layer to enhance the discrimination among various pre-cancerous and normal stages of cervical cancer and make the foundations for our future efforts to focus on in-vitro samples.

**Author Contributions:** Conceptualization, P.S. and A.P.; methodology, P.S. and P.P.; software, P.S.; validation, P.S., P.P. and S.S.; formal analysis, P.S.; investigation, P.S.; resources, A.P.; data curation, P.S. and S.S.; writing—original draft preparation, P.S.; writing—review and editing, P.S., P.P. and A.P.; supervision, A.P.; project administration, A.P. and N.N.; funding acquisition, A.P. and N.N. All authors have read and agreed to the published version of manuscript.

**Funding:** This research was funded by Board of Research in Nuclear Sciences(BRNS) of Department of Atomic Energy(DAE), India.

**Acknowledgments:** P.S. would like to acknowledge IIT Kanpur and UGC for giving me JRF/SRF scholarship and IIT Kanpur for lab facilities.

**Conflicts of Interest:** The authors declare no conflict of interest.

## References

1. Frank, S.A. *Dynamics of Cancer: Incidence, Inheritance, and Evolution*; Princeton University Press: Princeton, NJ, USA, 2007.
2. Ramanujam, N.; Mitchell, M.F.; Mahadevan, A.; Warren, S.; Thomsen, S.; Silva, E.; Richards-Kortum, R. In vivo diagnosis of cervical intraepithelial neoplasia using 337-nm-excited laser-induced fluorescence. *Proc. Natl. Acad. Sci. USA* **1994**, *91*, 10193–10197.
3. Liu, Q.; Ramanujam, N. Sequential estimation of optical properties of a two-layered epithelial tissue model from depth-resolved ultraviolet-visible diffuse reflectance spectra. *Appl. Opt.* **2006**, *45*, 4776–4790.
4. Tseng, T.Y.; Chen, C.Y.; Li, Y.S.; Sung, K.B. Quantification of the optical properties of two-layered turbid media by simultaneously analyzing the spectral and spatial information of steady-state diffuse reflectance spectroscopy. *Biomed. Opt. Express* **2011**, *2*, 901–914.
5. Farrell, T.J.; Patterson, M.S.; Wilson, B. A diffusion theory model of spatially resolved, steady-state diffuse reflectance for the noninvasive determination of tissue optical properties in vivo. *Med. Phys.* **1992**, *19*, 879–888.
6. Nair, M.S.; Ghosh, N.; Raju, N.S.; Pradhan, A. Determination of optical parameters of human breast tissue from spatially resolved fluorescence: A diffusion theory model. *Appl. Opt.* **2002**, *41*, 4024–4035.
7. Gupta, S.; Raja, V.S.; Pradhan, A. Simultaneous extraction of optical transport parameters and intrinsic fluorescence of tissue mimicking model media using a spatially resolved fluorescence technique. *Appl. Opt.* **2006**, *45*, 7529–7537.
8. Bays, R.; Wagnieres, G.; Robert, D.; Braichotte, D.; Savary, J.F.; Monnier, P.; van den Bergh, H. Clinical determination of tissue optical properties by endoscopic spatially resolved reflectometry. *Appl. Opt.* **1996**, *35*, 1756–1766.
9. Fawzi, Y.S.; Youssef, A.B.M.; El-Batanony, M.H.; Kadah, Y.M. Determination of the optical properties of a two-layer tissue model by detecting photons migrating at progressively increasing depths. *Appl. Opt.* **2003**, *42*, 6398–6411.
10. Kim, A.D.; Hayakawa, C.; Venugopalan, V. Estimating optical properties in layered tissues by use of the Born approximation of the radiative transport equation. *Opt. Lett.* **2006**, *31*, 1088–1090.

11. Sung, K.B.; Chen, H.H. Enhancing the sensitivity to scattering coefficient of the epithelium in a two-layered tissue model by oblique optical fibers: Monte Carlo study. *J. Biomed. Opt.* **2012**, *17*, 107003.
12. Wang, A.M.J.; Nammalvar, V.; Drezek, R.A. Experimental evaluation of angularly variable fiber geometry for targeting depth-resolved reflectance from layered epithelial tissue phantoms. *J. Biomed. Opt.* **2007**, *12*, 044011.
13. Utzinger, U.; Richards-Kortum, R.R. Fiber optic probes for biomedical optical spectroscopy. *J. Biomed. Opt.* **2003**, *8*, 121–148.
14. Nieman, L.; Myakov, A.; Aaron, J.; Sokolov, K. Optical sectioning using a fiber probe with an angled illumination-collection geometry: Evaluation in engineered tissue phantoms. *Appl. Opt.* **2004**, *43*, 1308–1319.
15. Sung, K.B.; Shih, K.W.; Hsu, F.W.; Hsieh, H.P.; Chuang, M.J.; Hsiao, Y.H.; Su, Y.H.; Tien, G.H. Accurate extraction of optical properties and top layer thickness of two-layered mucosal tissue phantoms from spatially resolved reflectance spectra. *J. Biomed. Opt.* **2014**, *19*, 077002.
16. Chang, V.T.C.; Cartwright, P.S.; Bean, S.M.; Palmer, G.M.; Bentley, R.C.; Ramanujam, N. Quantitative physiology of the precancerous cervix in vivo through optical spectroscopy. *Neoplasia* **2009**, *11*, 325–332.
17. Hornung, R.; Pham, T.; Keefe, K.; Berns, M.; Tadir, Y.; Tromberg, B. Quantitative near-infrared spectroscopy of cervical dysplasia in vivo. *Hum. Reprod.* **1999**, *14*, 2908–2916.
18. Kienle, A.; Patterson, M.S.; Dögnitz, N.; Bays, R.; Wagnières, G.; van Den Bergh, H. Noninvasive determination of the optical properties of two-layered turbid media. *Appl. Opt.* **1998**, *37*, 779–791.
19. Alexandrakis, G.; Farrell, T.J.; Patterson, M.S. Accuracy of the diffusion approximation in determining the optical properties of a two-layer turbid medium. *Appl. Opt.* **1998**, *37*, 7401–7409.
20. Reif, R.; A'Amar, O.; Bigio, I.J. Analytical model of light reflectance for extraction of the optical properties in small volumes of turbid media. *Appl. Opt.* **2007**, *46*, 7317–7328.
21. Zonios, G.; Dimou, A. Light scattering spectroscopy of human skin in vivo. *Opt. Express* **2009**, *17*, 1256–1267.
22. Palmer, G.M.; Ramanujam, N. Monte Carlo-based inverse model for calculating tissue optical properties. Part I: Theory and validation on synthetic phantoms. *Appl. Opt.* **2006**, *45*, 1062–1071.
23. Palmer, G.M.; Zhu, C.; Breslin, T.M.; Xu, F.; Gilchrist, K.W.; Ramanujam, N. Monte Carlo-based inverse model for calculating tissue optical properties. Part II: Application to breast cancer diagnosis. *Appl. Opt.* **2006**, *45*, 1072–1078.
24. Seo, I.; You, J.S.; Hayakawa, C.; Venugopalan, V. Perturbation and differential Monte Carlo methods for measurement of optical properties in a layered epithelial tissue model. *J. Biomed. Opt.* **2007**, *12*, 014030.
25. Yu, B.; Shah, A.; Nagarajan, V.K.; Ferris, D.G. Diffuse reflectance spectroscopy of epithelial tissue with a smart fiber-optic probe. *Biomed. Opt. Express* **2014**, *5*, 675–689.
26. Sharma, M.; Hennessy, R.; Markey, M.K.; Tunnell, J.W. Verification of a two-layer inverse Monte Carlo absorption model using multiple source-detector separation diffuse reflectance spectroscopy. *Biomed. Opt. Express* **2014**, *5*, 40–53.
27. Zhong, X.; Wen, X.; Zhu, D. Lookup-table-based inverse model for human skin reflectance spectroscopy: Two-layered Monte Carlo simulations and experiments. *Opt. Express* **2014**, *22*, 1852–1864.
28. Naglič, P.; Pernuš, F.; Likar, B.; Bürmen, M. Estimation of optical properties by spatially resolved reflectance spectroscopy in the subdiffusive regime. *J. Biomed. Opt.* **2016**, *21*, 095003.
29. Einstein, G.; Udayakumar, K.; Aruna, P.R.; Koteeswaran, D.; Ganesan, S. Diffuse reflectance spectroscopy for monitoring physiological and morphological changes in oral cancer. *Opt.-Int. J. Light Electron Opt.* **2016**, *127*, 1479–1485.
30. Hsieh, H.P.; Ko, F.H.; Sung, K.B. Hybrid method to estimate two-layered superficial tissue optical properties from simulated data of diffuse reflectance spectroscopy. *Appl. Opt.* **2018**, *57*, 3038–3046.
31. Wang, C.Y.; Kao, T.C.; Chen, Y.F.; Su, W.W.; Shen, H.J.; Sung, K.B. Validation of an Inverse Fitting Method of Diffuse Reflectance Spectroscopy to Quantify Multi-Layered Skin Optical Properties. *Photonics* **2019**, *6*, 61.
32. Chandrasekhar, S. The equation of transfer. In *Radiative Transfer*; Dover Publications: Mineola, NY, USA, 1960; pp. 1–53.
33. Wang, L.V.; Wu, H.i. *Biomedical Optics: Principles and Imaging*; John Wiley & Sons: Hoboken, NJ, USA, 2012.
34. Wang, L.; Jacques, S.L.; Zheng, L. MCML—Monte Carlo modeling of light transport in multi-layered tissues. *Comput. Methods Progr. Biomed.* **1995**, *47*, 131–146.

35. Tarvainen, T.; Vauhkonen, M.; Kolehmainen, V.; Arridge, S.R.; Kaipio, J.P. Coupled radiative transfer equation and diffusion approximation model for photon migration in turbid medium with low-scattering and non-scattering regions. *Phys. Med. Biol.* **2005**, *50*, 4913–4930, doi:10.1088/0031-9155/50/20/011.
36. Tarvainen, T.; Vauhkonen, M.; Kolehmainen, V.; Kaipio, J.P. Hybrid radiative-transfer-diffusion model for optical tomography. *Appl. Opt.* **2005**, *44*, 876–886, doi:10.1364/AO.44.000876.
37. Tarvainen, T.; Vauhkonen, M.; Arridge, S. Gauss–Newton reconstruction method for optical tomography using the finite element solution of the radiative transfer equation. *J. Quant. Spectrosc. Radiat. Transf.* **2008**, *109*, 2767–2778.
38. Balima, O.; Favennec, Y.; Boulanger, J.; Charette, A. Optical tomography with the discontinuous Galerkin formulation of the radiative transfer equation in frequency domain. *J. Quant. Spectrosc. Radiat. Transf.* **2012**, *113*, 805–814.
39. Tang, J.; Han, B.; Han, W.; Bi, B.; Li, L. Mixed total variation and regularization method for optical tomography based on radiative transfer equation. *Comput. Math. Methods Med.* **2017**, *2017*, 2953560.
40. Addoum, A.; Farges, O.; Asllanaj, F. Optical properties reconstruction using the adjoint method based on the radiative transfer equation. *J. Quant. Spectrosc. Radiat. Transf.* **2018**, *204*, 179–189.
41. Boas, D.A.; Brooks, D.H.; Miller, E.L.; DiMarzio, C.A.; Kilmer, M.; Gaudette, R.J.; Zhang, Q. Imaging the body with diffuse optical tomography. *IEEE Signal Process. Mag.* **2001**, *18*, 57–75.
42. Pogue, B.W.; McBride, T.O.; Prewitt, J.; Österberg, U.L.; Paulsen, K.D. Spatially variant regularization improves diffuse optical tomography. *Appl. Opt.* **1999**, *38*, 2950–2961.
43. Corlu, A.; Choe, R.; Durduran, T.; Rosen, M.A.; Schweiger, M.; Arridge, S.R.; Schnall, M.D.; Yodh, A.G. Three-dimensional in vivo fluorescence diffuse optical tomography of breast cancer in humans. *Opt. Express* **2007**, *15*, 6696–6716.
44. Culver, J.P.; Durduran, T.; Furuya, D.; Cheung, C.; Greenberg, J.H.; Yodh, A. Diffuse optical tomography of cerebral blood flow, oxygenation, and metabolism in rat during focal ischemia. *J. Cereb. Blood Flow Metab.* **2003**, *23*, 911–924.
45. Corlu, A.; Choe, R.; Durduran, T.; Lee, K.; Schweiger, M.; Arridge, S.R.; Hillman, E.M.; Yodh, A.G. Diffuse optical tomography with spectral constraints and wavelength optimization. *Appl. Opt.* **2005**, *44*, 2082–2093.
46. Hielscher, A.; Bluestone, A.; Abdoulaev, G.; Klose, A.; Lasker, J.; Stewart, M.; Netz, U.; Beuthan, J. Near-infrared diffuse optical tomography. *Dis. Markers* **2002**, *18*, 313–337.
47. Shimada, M.; Sato, C.; Hoshi, Y.; Yamada, Y. Estimation of the absorption coefficients of two-layered media by a simple method using spatially and time-resolved reflectances. *Phys. Med. Biol.* **2009**, *54*, 5057.
48. Bravo, J.J.; Paulsen, K.D.; Roberts, D.W.; Kanick, S.C. Sub-diffuse optical biomarkers characterize localized microstructure and function of cortex and malignant tumor. *Opt. Lett.* **2016**, *41*, 781–784.
49. Jaillon, F.; Zheng, W.; Huang, Z. Beveled fiber-optic probe couples a ball lens for improving depth-resolved fluorescence measurements of layered tissue: Monte Carlo simulations. *Phys. Med. Biol.* **2008**, *53*, 937.
50. Arifler, D.; MacAulay, C.E.; Follen, M.; Richards-Kortum, R.R. Spatially resolved reflectance spectroscopy for diagnosis of cervical precancer: Monte Carlo modeling and comparison to clinical measurements. *J. Biomed. Opt.* **2006**, *11*, 064027.

**Publisher’s Note:** MDPI stays neutral with regard to jurisdictional claims in published maps and institutional affiliations.



© 2020 by the authors. Licensee MDPI, Basel, Switzerland. This article is an open access article distributed under the terms and conditions of the Creative Commons Attribution (CC BY) license (<http://creativecommons.org/licenses/by/4.0/>).